

A Numerical Study of Typhoon Megi (2010). Part II: Eyewall Evolution Crossing the Luzon Island

HUI WANG^a AND YUQING WANG^{a,b,c}

^aState Key Laboratory of Severe Weather, Chinese Academy of Meteorological Sciences, Beijing, China

^bInternational Pacific Research Center, University of Hawai'i at Mānoa, Honolulu, Hawaii

^cDepartment of Atmospheric Sciences, University of Hawai'i at Mānoa, Honolulu, Hawaii

(Manuscript received 15 November 2019, in final form 10 October 2020)

ABSTRACT: Typhoon Megi (2010) experienced drastic eyewall structure changes when it crossed the Luzon Island and entered the South China Sea (SCS), including the contraction and breakdown of the eyewall after landfall over the Luzon Island, the formation of a new large outer eyewall accompanied by reintensification of the storm after it entered the SCS, and the appearance of a short-lived small inner eyewall. These features were reproduced reasonably well in a control simulation using the Advanced Weather Research and Forecasting (ARW-WRF) Model. In this study, the eyewall processes of the simulated Megi during and after landfall have been analyzed. Results show that the presence of the landmass of the Luzon Island increased surface friction and reduced surface enthalpy flux, causing the original eyewall to contract and break down and the storm to weaken. The formation of the new large eyewall results mainly from the axisymmetrization of outer spiral rainbands after the storm core moved across the Luzon Island and entered the SCS. The appearance of the small inner eyewall over the SCS was due to the increased surface enthalpy flux and the revival of convection in the central region of the storm core. In a sensitivity experiment with the mesoscale mountain replaced by flat surface over the Luzon Island, a new large outer eyewall formed over the western Luzon Island with its size about one-third smaller after the storm entered the SCS than that in the control experiment with the terrain over the Luzon Island unchanged.

KEYWORDS: Hurricanes/tropical cyclones; Tropical cyclones; Orographic effects; Numerical analysis/modeling

1. Introduction

One of the distinct features of an intense tropical cyclone (TC) is the eyewall structure characterized by a nearly closed convective ring with the strongest swirling wind and heavy rainfall. It is generally believed that the evolution of the eyewall structure is often responsible for the intensity change of a TC. In particular, as pointed out by Wang and Wu (2004), the TC intensity change induced by any external forcing is predominantly determined by how the eyewall processes respond to the external forcing, such as vertical wind shear and island orography. Therefore, studies of the eyewall processes can help to improve our understanding of TC structure and intensity changes.

One of the most pronounced eyewall processes is the eyewall replacement associated with the formation of a concentric eyewall structure (e.g., Willoughby et al. 1982; Willoughby and Black 1996; Houze et al. 2007; Kuo et al. 2009; Kossin and Sitkowski 2009; Sitkowski et al. 2011; Huang et al. 2012; Didlake and Houze 2011; Didlake et al. 2018; Wang et al. 2016, 2019). In this scenario, a secondary (outer) eyewall forms outside of the primary (inner) eyewall and intensifies while the inner eyewall weakens and is replaced by the intensifying outer eyewall. This process is often accompanied by large intensity changes, first weakening and then reintensifying, leading to a larger inner-core size increase of the TC (Maclay et al. 2008; Sitkowski et al. 2011; Wang 2009, 2012). A similar TC intensity change can be caused by the so-called partial eyewall breakdown and recovery triggered by the interaction between the

eyewall and outer spiral rainbands studied in the simulation of an idealized TC by Wang (2002a,b).

Barotropic instability is considered responsible for the formation of mesovortices in the eyewall and the polygonal eyewall structure (Schubert et al. 1999; Kossin and Schubert 2001; Rozoff et al. 2009; Hendricks et al. 2009). These transient asymmetric flows are responsible for the horizontal mixing of potential vorticity (PV) and angular momentum between the eye and the eyewall, causing distinct changes in the kinematic and thermodynamic structure of the eye and eyewall (Schubert et al. 1999; Kossin and Eastin 2001; Hendricks and Schubert 2010). Knaff et al. (2003) suggested that the asymmetric mixing between the eye and eyewall could contribute to the formation of the annular hurricanes, a category of hurricanes being more axisymmetric with a circular large eye surrounded by a uniform wide convective ring with suppressed activity of spiral rainbands outside the eyewall. These internally generated asymmetries in the inner core may limit the TC intensity (Yang et al. 2007).

Another quite interesting eyewall process documented and studied earlier is the one related to the effects of island topography, such as the Luzon Island and Taiwan Island in the western Pacific and Haiti, Jamaica and eastern Cuba in the North Atlantic (Brand and Bleloch 1973; Hawkins 1983; Wu et al. 2003, 2009; Chou et al. 2011; Hsu et al. 2013; Wu 2013; Wei 2014; Tang and Chan 2014, 2016). Most studies have focused on the effects of island landmass and terrain on TC motion, including track discontinuity and deflection, rainfall distribution, and structure changes by Taiwan Island (e.g., Wu and Kuo 1999; Lin et al. 2002, 2006; Yang et al. 2008; Huang et al. 2011). Because of the high central mountain ranges of

Corresponding author: Yuqing Wang, yuqing@hawaii.edu

Taiwan Island, most TCs significantly weaken after they make landfall over the Taiwan Island, and the terrain over the Taiwan Island mainly causes track deflection and discontinuity, and heavy rainfall enhancement over the windward slope of mountains.

In contrast to the Taiwan Island, the Luzon Island in the northern Philippines has a much smaller size (comparable to the inner-core size of a TC) with height of about 1500 m (Fig. 1). Its effect on TC motion is generally minor while it can cause significant eyewall structure changes (Brand and Bleloch 1973; Chou et al. 2011; Lin and Chou 2018). Based on aircraft reconnaissance data during 1960–70, Brand and Bleloch (1973) found that TCs passing the islands of the Philippines generally experienced weakening while on average above 50% increase in eye diameter. This common feature of TCs passing the Luzon Island was recently revisited by Chou et al. (2011) based on satellite observations during 2000–10. They found that at least 87% of TCs passing the Philippine islands showed an increase in the radius of the eyewall during landfall and 57% of TCs showed an eyewall contraction after they reentered the ocean as they re-intensified. More recently, Lin and Chou (2018) examined changes in the radius of storm wind with 30 kt ($1 \text{ kt} \approx 0.51 \text{ m s}^{-1}$) in TCs crossing the Philippine islands based on the best track data of the Japan Meteorological Agency. They found that over 60% of TCs crossing the islands experienced an increase in this radius during 1998 and 2015.

The above-documented eyewall evolution of TCs passing the Luzon Island was first studied by Wu et al. (2003, 2009) for Typhoon Zeb (1998) based on high-resolution cloud-resolving simulations. In Wu et al. (2003), the observed eyewall evolution was reproduced in a control simulation including both dynamical and thermodynamic details. Wu et al. (2009) further conducted a series of numerical experiments and demonstrated that the presence of the Luzon Island played a critical role in causing the observed eyewall evolution in Typhoon Zeb. They showed that the eyewall replacement in Zeb was triggered by the mesoscale landmass and terrain variation with a horizontal scale similar to the core size of the storm. In Zeb, the original eyewall contracted and broke down after landfall because of the enhanced surface friction. The outer eyewall was triggered by convective rainbands near the western coastal region of the Luzon Island and formed as a result of axisymmetrization well after the dissipation of the original eyewall convection.

In the Typhoon Megi (2010) case, a similar eyewall replacement process occurred. Different from the majority of TCs passing the Luzon Island, an inner eyewall appeared inside the newly formed larger outer eyewall after the storm entered the SCS, showing a classic double eyewall structure. However, this is very different from the formation of a classic concentric eyewall as mentioned above. In Typhoon Megi, the original eyewall weakened and disappeared after it made landfall over the Luzon Island. A new large eyewall formed later as a result of the axisymmetrization of strong outer spiral rainbands. A small inner eyewall formed radially inside the big outer eyewall after Megi entered and moved over the SCS. The formation of this double eyewall structure is quite unique because the classic double eyewall structure results from the formation of a secondary (outer) eyewall outside an existing primary (inner) eyewall.

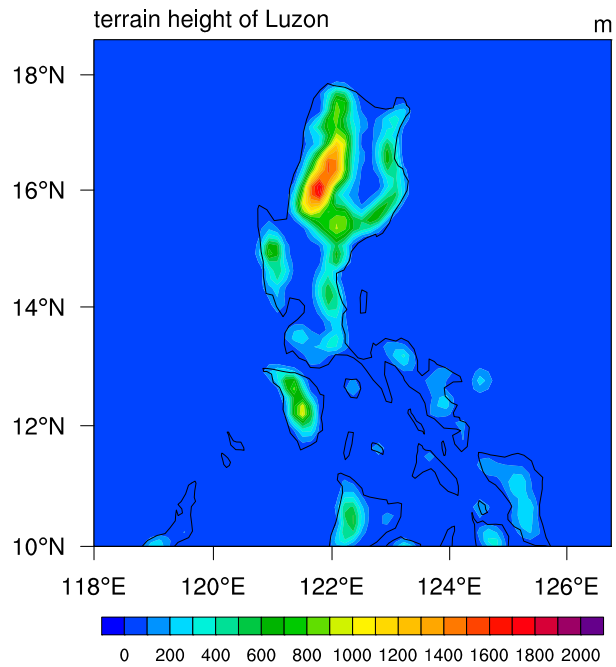


FIG. 1. Terrain height (m) of the Luzon Island that was used in the control simulation.

The purpose of this study is to understand the eyewall evolution in the simulated Megi when it passed the Luzon Island. Three eyewall stages, namely the weakening, breakdown of the original eyewall at landfall, the formation of a new large outer eyewall, and the appearance of the small inner eyewall, are analyzed based on the control simulation as documented in Wang and Wang (2014, hereinafter Part I). Details of the control simulation and the analysis associated with the rapid intensification of the simulated Megi before its landfall over the Luzon Island can be found in Part I. The roles of terrain over the Luzon Island and the landmass of Luzon Island in the eyewall evolution of Megi are evaluated based on sensitivity experiments with either the terrain replaced by a flat surface or the Luzon Island replaced completely by an ocean surface. The rest of the paper is organized as follows. An overview of the eyewall evolution of Typhoon Megi in observations and numerical experiments is given in section 2. The weakening and dissipation of the original eyewall convection after landfall over the Luzon Island are analyzed in section 3. Section 4 focuses on the formation processes of a new large eyewall after the breakdown and dissipation of the original eyewall. The appearance of the small inner eyewall after the storm entered the SCS is discussed in section 5. Major findings are drawn in the last section.

2. An overview of the eyewall evolution and numerical simulations

a. An overview of the eyewall evolution of Typhoon Megi crossing the Luzon Island

Typhoon Megi (2010) was the most powerful and longest-lived TC over the western North Pacific in 2010. Megi exhibited

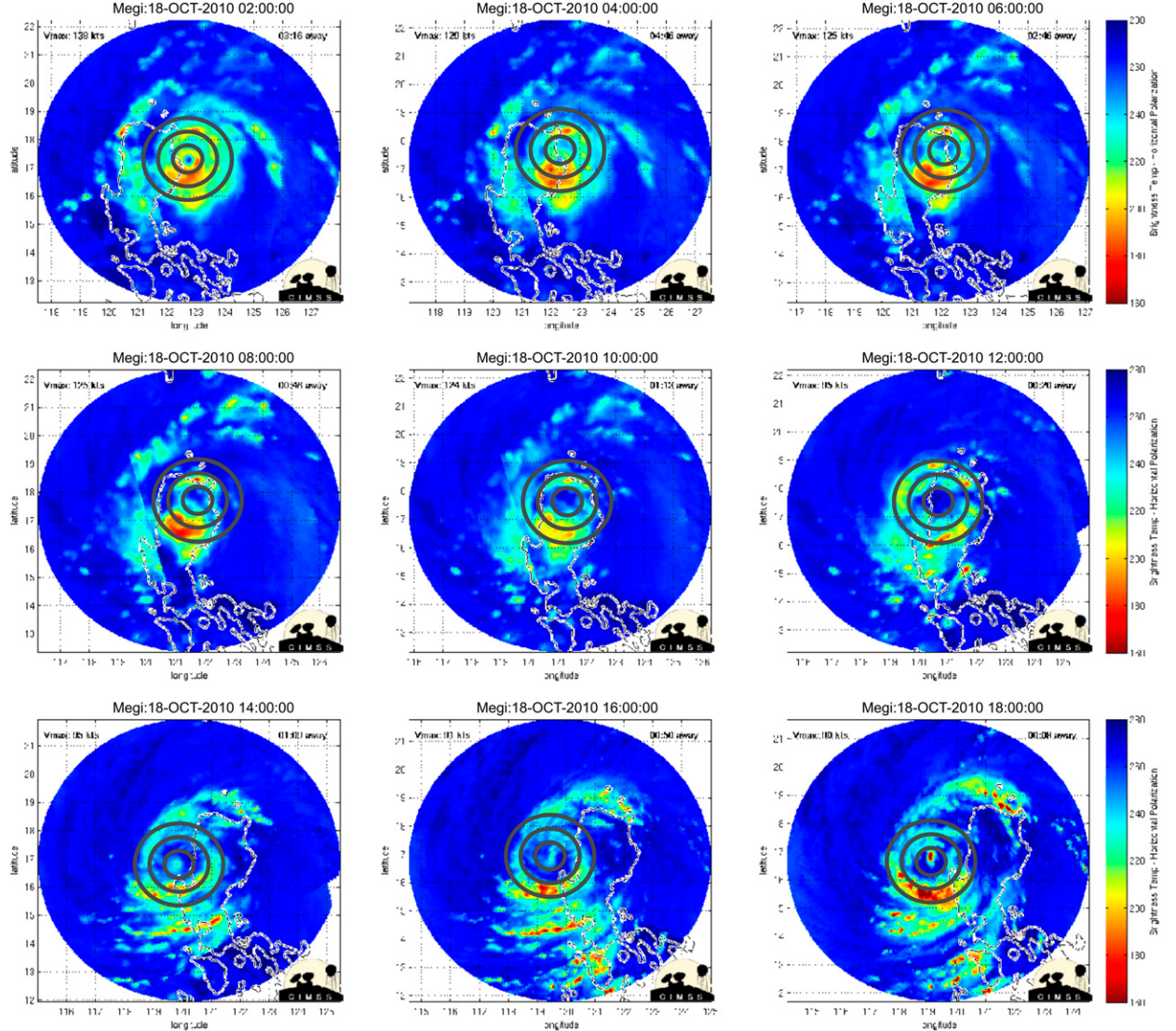


FIG. 2. The MIMIC-IR brightness temperature (shading; K) at given times for Typhoon Megi (2010). The upper-left corner of each panel shows the JTWC-reported maximum sustained winds interpolated in time, and the upper-right corner of each panel shows the time to the nearest actual image either before or after (whichever is closer). The MIMIC product is a synthetic blend of tropical cyclone imagery with 15-min interval from five low-Earth-orbiting satellite instruments: the DMSP-13/14/15 SSM/I (85-GHz channel), the TRMM TMI (89-GHz channel), and the *Aqua* AMSR-E (85-GHz channel). The three circles in each panel are the range of 0.5° , 1° , and 1.5° from the storm center.

a drastic structural change after it crossed the Luzon Island in the northern Philippines and entered the SCS as already mentioned in Part I. Here only some major features are briefly restated. After its rapid intensification to the east of the Philippines, Megi made landfall over the Luzon Island. Its eyewall experienced contraction, breakdown, and eventually dissipation processes when it crossed the Luzon Island, which can be seen from the brightness temperature during 0200–1800 UTC 18 October 2010 shown in Fig. 2. When Megi moved across the Luzon Island, outer rainbands remained strong even though its inner-core intensity substantially weakened. After Megi entered the SCS, strong outer rainbands experienced a

quick axisymmetrization and contraction, leading to the formation of a new large eyewall (1200 UTC 18 October in Fig. 2) and a reintensification of the storm. Similar features have been previously described for storms that crossed the Luzon Island from both observations and numerical simulations (Wu et al. 2003, 2009; Chou et al. 2011).

An interesting feature is the appearance of a small inner eyewall shortly after the formation of the new large (outer) eyewall in Megi when it entered and moved over the SCS (1400–1800 UTC 18 October in Fig. 2). The small inner eyewall weakened after about 7–9 h as a result of the intensification and contraction of the large outer eyewall. The appearance of the

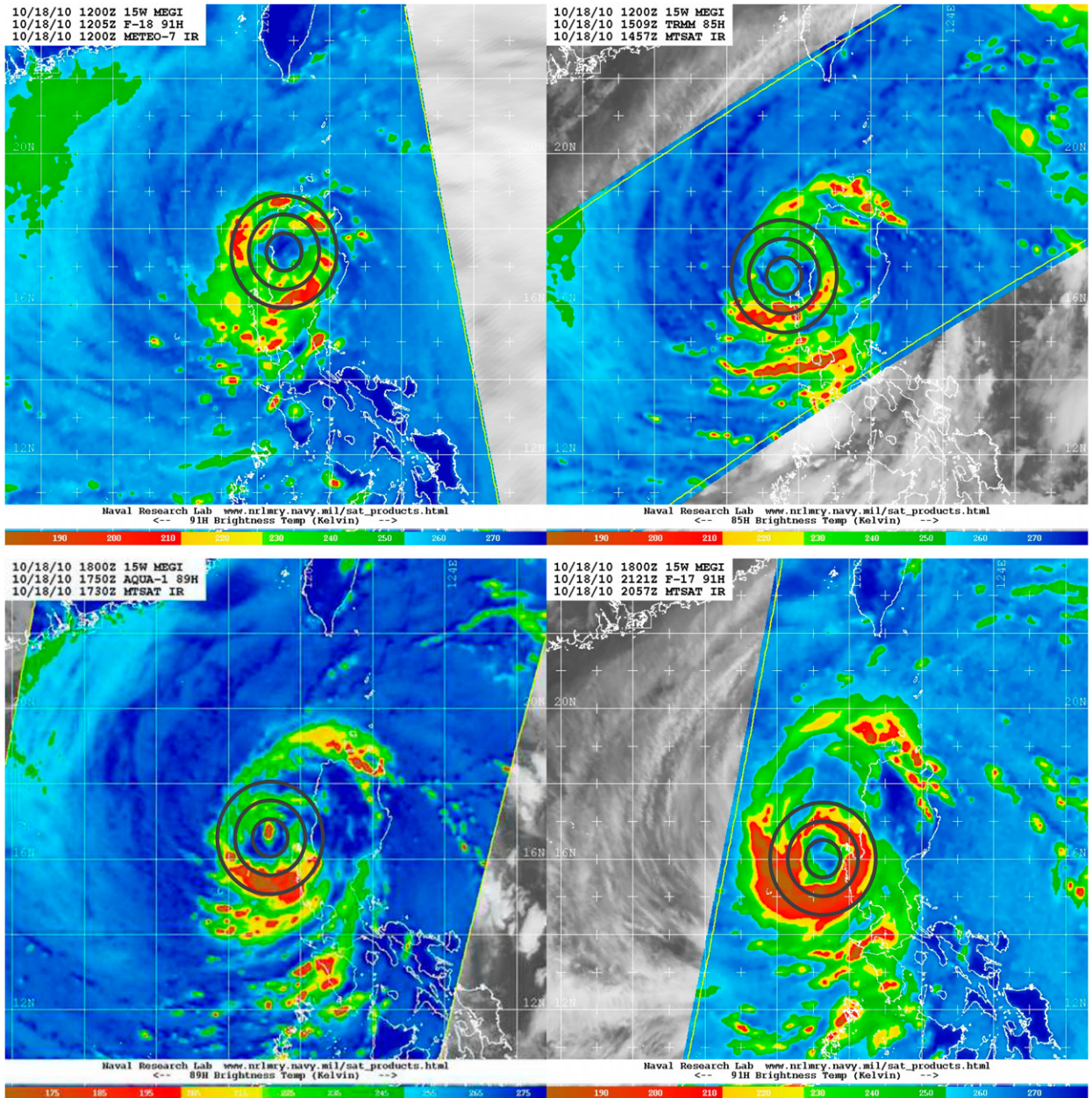


FIG. 3. The SSMI-85–91-GHz satellite images at four given times, showing the redevelopment of the inner eyewall-like structure after Typhoon Megi (2010) crossed the Luzon Island and entered the SCS. The three circles in each panel are the range of 0.5° , 1° , and 1.5° from the storm center.

small inner eyewall can be easily identified in our high-resolution control simulation as we will discuss in the next sections. The appearance of the small inner eyewall generally could not be well resolved from visible and infrared satellite observations because of the small size and asymmetric distribution of the inner eyewall and the relatively coarse spatial resolution of satellite data and the thick high cloud canopy over the storm. Nevertheless, the 85–91 GHz channel aboard the SSM/I, which has both polarizations (horizontal “H” and vertical “V”), gives images showing similar appearance of the

small inner eyewall (Fig. 3). However, because of its 0.25° latitude horizontal resolution, SSMI-85–91 GHz can only show some convective activity near the storm center but it could not resolve well the small inner eyewall of Megi with 6-h interval (Fig. 3). Nevertheless, there is still observational evidence for the simulated double eyewall structure discussed later.

b. Numerical simulations

All numerical simulations discussed in this study for Typhoon Megi were performed using the Advanced Research Weather

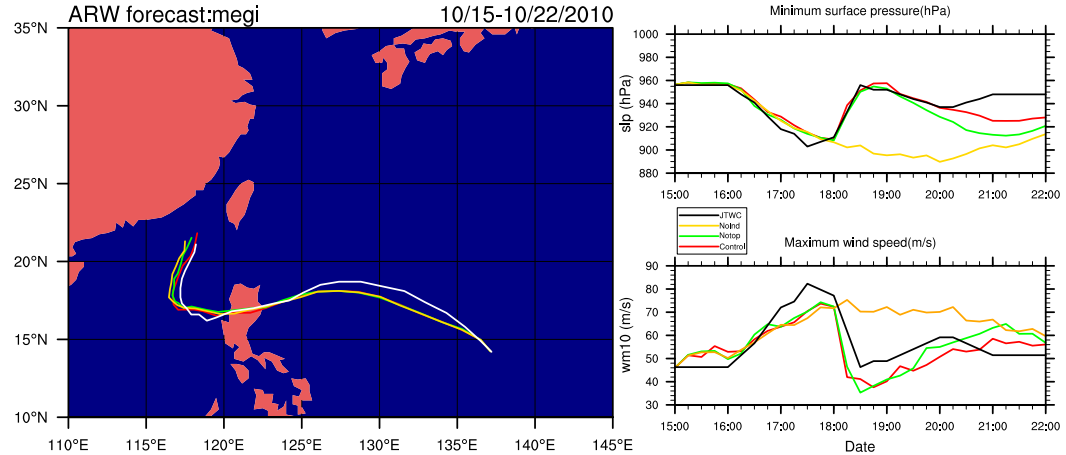


FIG. 4. (left) Track and (top right) intensity evolution in terms of the central sea level pressure (hPa), and (bottom right) the maximum 10-m wind speed (m s^{-1}) from the JTWC best track data and from the control simulation in Wang and Wang (2014) and two sensitivity experiments in this study. The date is in the format of day:hour in the right panels.

Research and Forecasting (ARW-WRF) Model, version 3.3.1 (Skamarock et al. 2008). Details of the model settings can be found in Wang et al. (2013) and are not repeated here. As indicated in Part I, the overall structure change, including the development of a new large eyewall and the appearance of the small inner eyewall after Megi entered the SCS, was reproduced reasonably well in the control simulation. In this study, two sensitivity experiments were conducted. As in the control simulation, both experiments were performed for 168 h from 0000 UTC 15 October to 0000 UTC 22 October 2010. In both sensitivity experiments, the same initial conditions as used in the control simulation were used. The only differences were the lower boundary conditions. In one experiment (Notop), the terrain height over the Luzon Island was reset to be 0.2 m, that is, the Luzon Island was treated as a flat island, but with no changes to the land surface properties. In the other sensitivity experiment (Nolnd), the Luzon Island was replaced by the ocean surface with the sea surface temperature (SST) obtained by interpolating SSTs in the surrounding oceans from the National Centers for Environmental Prediction Global Forecast System final analysis (FNL). These two experiments were designed to help understand the individual roles of the island terrain and landmass of Luzon Island in the eyewall evolution of the simulated Typhoon Megi in the control simulation and in observation.

Figure 4 compares the tracks and intensities from the control simulation and two sensitivity experiments of Typhoon Megi with those from the best track data of the Joint Typhoon Warning Center (JTWC). All experiments simulated the storm track reasonably well compared with the JTWC best track. The differences in the simulated tracks among the three simulations were very small. Only some noticeable differences appeared after the storm entered the SCS and moved westward and then turned northward in experiment Nolnd (Fig. 4, left panel). The results thus suggest that the overall effects of the island terrain and landmass of the Luzon Island on Megi's motion were marginal. The simulated storm intensity in the experiment

with a flat island over the Luzon Island was very similar to that in the control simulation and compared reasonably well with that of the JTWC best track (Figs. 4, right panels). This suggests that the terrain over the Luzon Island had little effects on the simulated storm intensity throughout the week-long simulation, although some nonnegligible differences appeared well after the storm passed the Luzon Island. In sharp contrast, the storm in experiment Nolnd showed no weakening when it crossed the region of Luzon Island because the region was replaced by an ocean surface. This demonstrates that the weakening of the storm resulted mainly from the increased surface friction and the largely reduced surface enthalpy flux after the storm made landfall over the Luzon Island. This is consistent with the results reported earlier by Wu et al. (2009) for Typhoon Zeb (1998). We will show below that the eyewall evolution was considerably affected by both the terrain and landmass of Luzon Island.

3. Eyewall contraction, breakdown, and dissipation over the Luzon Island

Figure 5 shows the evolution of the simulated radar reflectivity at the lowest model level in the control simulation of Megi prior to landfall, during the landfall, and after it entered the SCS. The simulated Megi experienced an eyewall contraction, and the eyewall convection substantially weakened over the land to the front of the storm. As the storm moved inland, the eye shrank and then gradually filled with some shallow convection by 0900 UTC 18 October. Shortly later, the small eyewall filled in less than 2 h. The inner core convection disappeared (Fig. 5e), and the storm was characterized by outer spiral rainbands when the storm center was over the land. Deep convection remained strong on the windward side while a rain shadow (almost precipitation-free area) appeared on the leeward side of the high mountain. By 1100 UTC 18 October, the eyewall substantially weakened and showed a semicircle eyewall structure in radar reflectivity with high

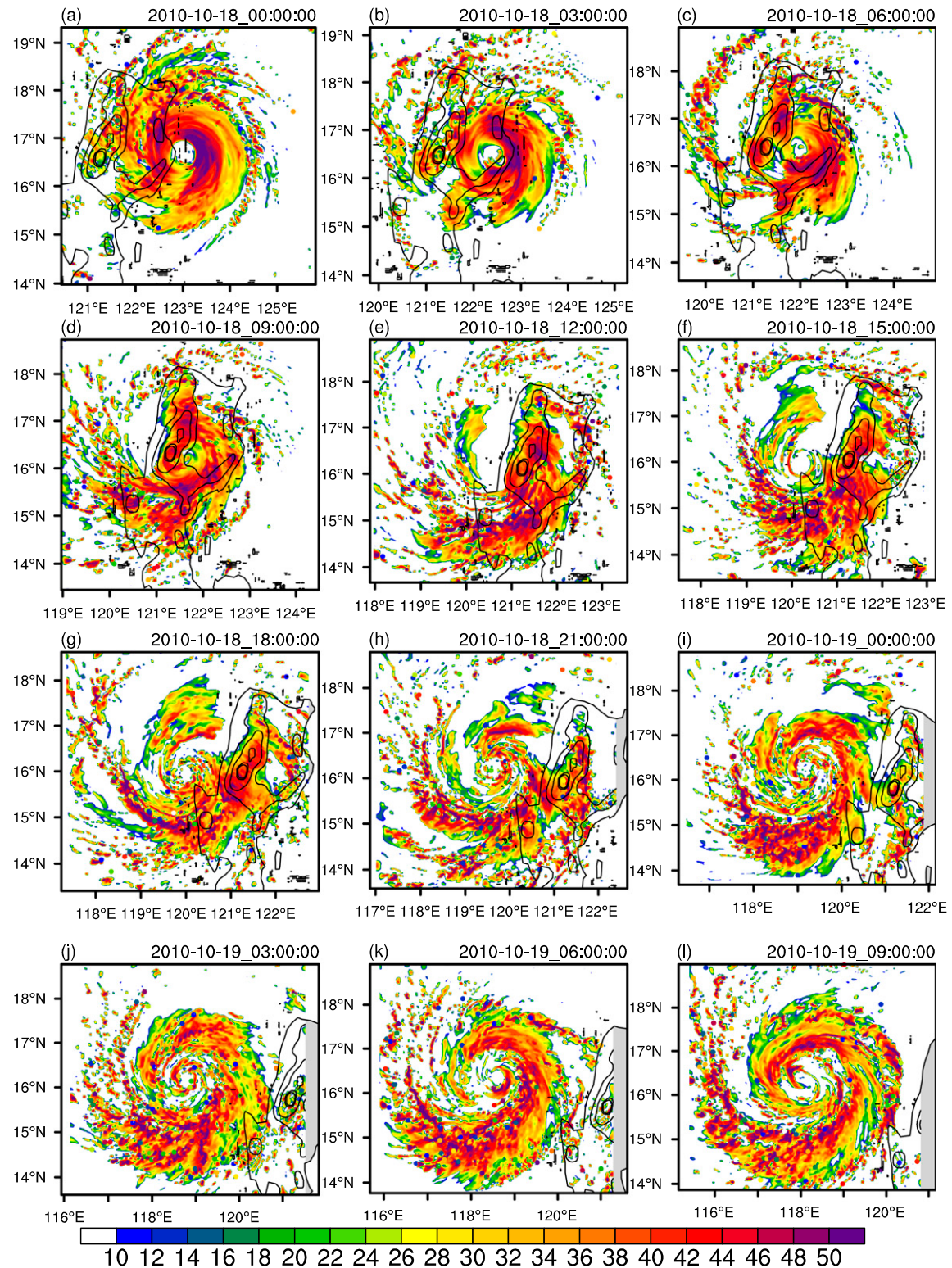


FIG. 5. Radar reflectivity at the lowest model level (shaded; dBZ) for the control simulation of Typhoon Megi, showing the structure change of the storm before, during, and after its landfall over the Luzon Island in the northern Philippines. The black contours on the Luzon Island indicate the height of the terrain, with 500-m interval.

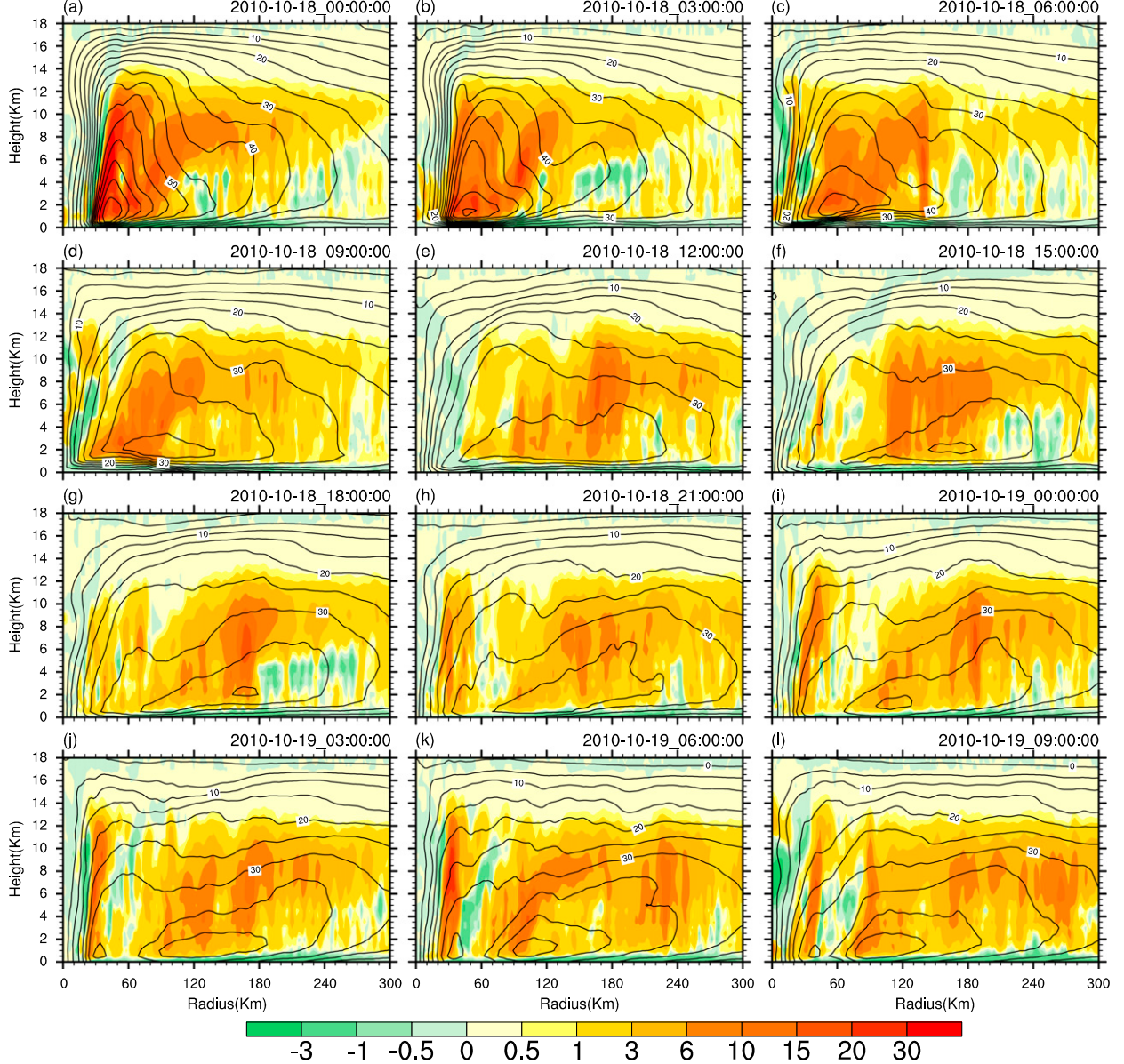


FIG. 6. The azimuthal mean tangential wind (contours; m s^{-1}) and diabatic heating rate (shading; K h^{-1}) at the time given at the top of each panel, showing the time evolution of eyewall convection and the associated azimuthal mean tangential wind in the control simulation.

reflectivity to the east in the eyewall. The 9-h period from 0300 to 1200 UTC 18 October can be considered as the eyewall contraction, (partial eyewall) breakdown and dissipation stage of the simulated Megi over the Luzon Island (Figs. 5b–e).

The eyewall contraction, breakdown, and dissipation inferred from the model radar reflectivity in Fig. 5 can also be seen from the evolution of the azimuthally averaged tangential wind and diabatic heating rate as shown in Fig. 6. At 0000 UTC 18 October when the simulated Megi was approaching the Luzon Island (Fig. 5a), large condensational heating occurred in the eyewall near the radius of 40 km (Fig. 6a). In the following 6–9 h during which the storm eyewall contracted, broke

down and dissipated, the condensational heating rate in the inner-core region within a radius of 100 km from the storm center weakened greatly, indicating that eyewall convection became less vertically penetrative and loosely organized. At both 0600 and 0900 UTC 18 October, diabatic heating in the eyewall occurred near the storm center with the maximum heating in the upper troposphere by 0900 UTC (Fig. 6d). This suggests that the small eyewall in Fig. 5d corresponded to stratiform precipitation as the low-level eyewall structure weakened and dissipated by 1200 UTC 1800 October (Fig. 6e).

The azimuthal mean tangential wind was strong (exceed 75 m s^{-1}) in the boundary layer under the eyewall near the

radius of 40 km prior to landfall of the storm center (Fig. 6a). After landfall, the azimuthal mean tangential wind continuously weakened. Interestingly, the azimuthal mean tangential winds showed little weakening and even slightly increasing outside of the radius of 150 km along with continuous weakening in the inner core region (Figs. 6c–e). The inner-core tangential wind maximum disappeared shortly after its corresponding convective activity dissipated by 1400 UTC 18 October (Figs. 6e,f). This can be more easily seen from the azimuthal mean tangential wind at the altitude of 1.5 km as shown in Fig. 7 even though the tangential wind looks quite uniform in the lower troposphere by 1200 UTC 18 October (Fig. 6e) and it is even hard to find the radius of maximum wind (RMW). Note that the maximum tangential winds in the control simulation remained over 33 m s^{-1} when the storm moved over the Luzon Island, which is about 10 m s^{-1} weaker than that in the JTWC best track (Fig. 3c). This is partially because the peak intensity of the simulated storm prior to landfall was also weaker than the observed Megi.

With the terrain height over the Luzon Island reduced to a flat surface in experiment Notop, the eyewall contracted in a similar way to that we see in the control simulation during the first 9 h on 18 October (Fig. 8). Later on, different evolutions of the storm structure in experiment Notop occurred over the Luzon Island. As a result of the continuous contraction of the inner part of the eyewall, a secondary maximum was spun up near 100–120-km radius. This gives rise to an appearance of the double eyewall structure, which maintained for about 26 h until 1000 UTC 19 October when the convective ring in the inner eyewall broke down and the outer eyewall strengthened and became more axisymmetric. The inner eyewall had its own local maximum in the azimuthal mean tangential wind in the boundary layer accompanied with the convective ring, very similar to the classic double eyewall structure, while the maximum wind speed in the inner eyewall was smaller than that in the outer eyewall (Fig. 9). The different eyewall evolution in Notop from that in the control experiment demonstrates that the eyewall evolution of the simulated Megi during its landfall was closely related to the interaction of the eyewall with the narrow mountain over the western Luzon Island. The mountain indeed caused the breakdown of the inner part of the eyewall, which had a similar horizontal scale to the mountain.

Although the eyewall evolution in experiment Notop over the SCS showed some similarity to that in the control simulation, the RMW and the eyewall size in experiment Notop were both smaller (Figs. 5 and 7–9). For example, the RMW in experiment Notop was about 60 km after 1000 UTC 19 October (Fig. 9), about 20 km (or one-third) smaller than that in the control simulation (Fig. 7). Therefore, the above results demonstrate that in addition to the effect of the landmass of Luzon Island, the mesoscale mountain over the western Luzon Island also contributed to the increase in the eyewall size of the simulated storm.

The orographic effect of the narrow mountain over the western Luzon Island can be clearly seen from a comparison of the zonal-vertical cross section through the simulated storm center in the control experiment with that in experiment Notop (Fig. 10). In the control experiment (Fig. 10a), by the time

when the storm core was approaching the mountain, high reflectivity and thus convection was blocked on the eastern slope of the mountain, namely on windward side in this case. On the leeward side, that is on the western slope of the mountain, reflectivity is generally low. Farther to the west was high reflectivity associated with an outer spiral rainband formed earlier over the SCS. In sharp contrast, with the terrain replaced by a flat surface (Fig. 10d), the inner eyewall was filled with relatively high reflectivity, which was surrounded by an outer eyewall with deep convection to the east and shallow clouds to the west of the storm center. Therefore, it is the orographic effect of the western Luzon Island that led to the breakdown and dissipation of the original eyewall of the simulated Megi although its effect on the overall intensity evolution of the simulated storm is marginal.

4. Formation of the new large eyewall

The formation of the new large eyewall after the storm entered the SCS can be traced back to the landfall of the simulated Megi. As seen from Fig. 5, an outer spiral rainband formed over the SCS west of the Luzon Island when the storm just made landfall (Figs. 5b,c), which then intensified and spiraled cyclonically and became a strong rainband to the south and southeast of the eyewall until 2100 UTC 18 October (Fig. 5h). This outer rainband then further intensified as a result of the interaction between the TC outer circulation and the island landmass. By 1200 UTC 18 October (Fig. 5e), a new outer spiral rainband formed northwest of the storm center. In contrast to the previous outer rainband, this new rainband showed a quasi-stationary nature and intensified locally. Later on, this rainband connected to the previous rainband from the southeast and became part of the newly formed large eyewall with its own RMW of about 180 km by 1800 UTC 18 October (Fig. 5g) after the storm entered the SCS. This new large eyewall experienced a contraction with the RMW decreased to 80 km by 2000 UTC 19 October (Figs. 5 and 7).

The formation of the new large eyewall can thus be considered being a result of the axisymmetrization of the outer spiral rainbands. This can be clearly seen from the azimuthal mean tangential wind and diabatic heating rate in Fig. 6. Both the azimuthal mean tangential wind and diabatic heating rate in the original eyewall weakened substantially after the simulated storm made landfall over the Luzon Island, in particular when the storm crossed the mesoscale terrain over the western Luzon Island (Figs. 6b–d). Meanwhile, the azimuthal mean tangential wind showed an outward expansion in the mid- to lower troposphere along with the substantially increasing diabatic heating rate. This indicates an eyewall replacement process by 1200–1800 UTC 18 October in terms of both the azimuthal mean tangential wind in the boundary layer and eyewall convection (Figs. 6 and 7). Note that an inner eyewall structure with convection appeared within the new large eyewall several hours after the storm entered the SCS (Figs. 5f and 6f), showing another double eyewall structure, a topic will be further discussed in the next section.

The above results suggest that the key to the formation of the new large eyewall is the initiation of outer spiral rainbands

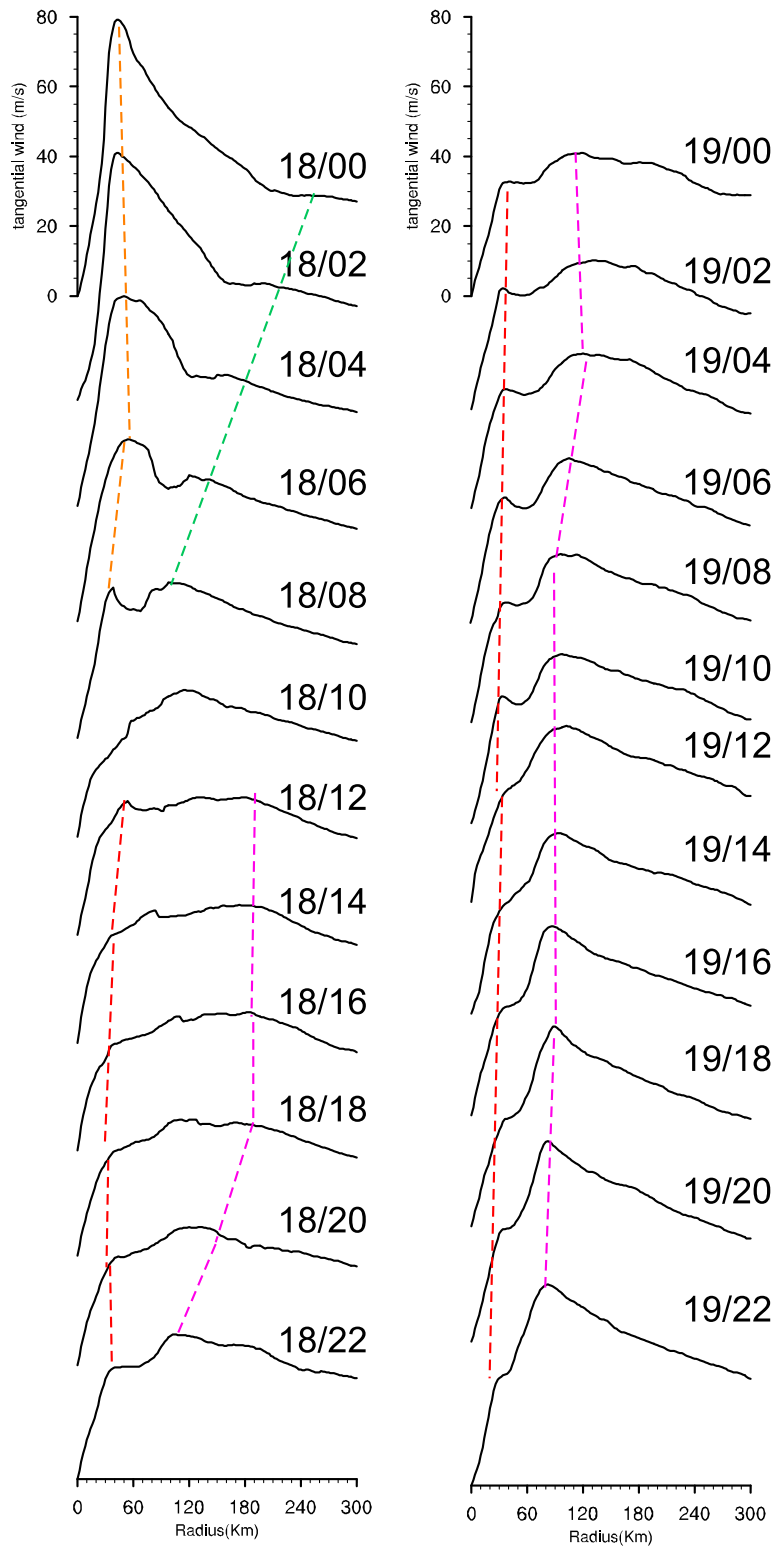


FIG. 7. Radial profiles of the azimuthal mean tangential winds at the altitude of 1.5 km in the control simulation; the orange dashed line indicates the original eyewall before landfall, the red dashed line indicates the appearance of the inner eyewall after landfall, and the green and magenta dashed lines indicate the evolution with the outer eyewall.

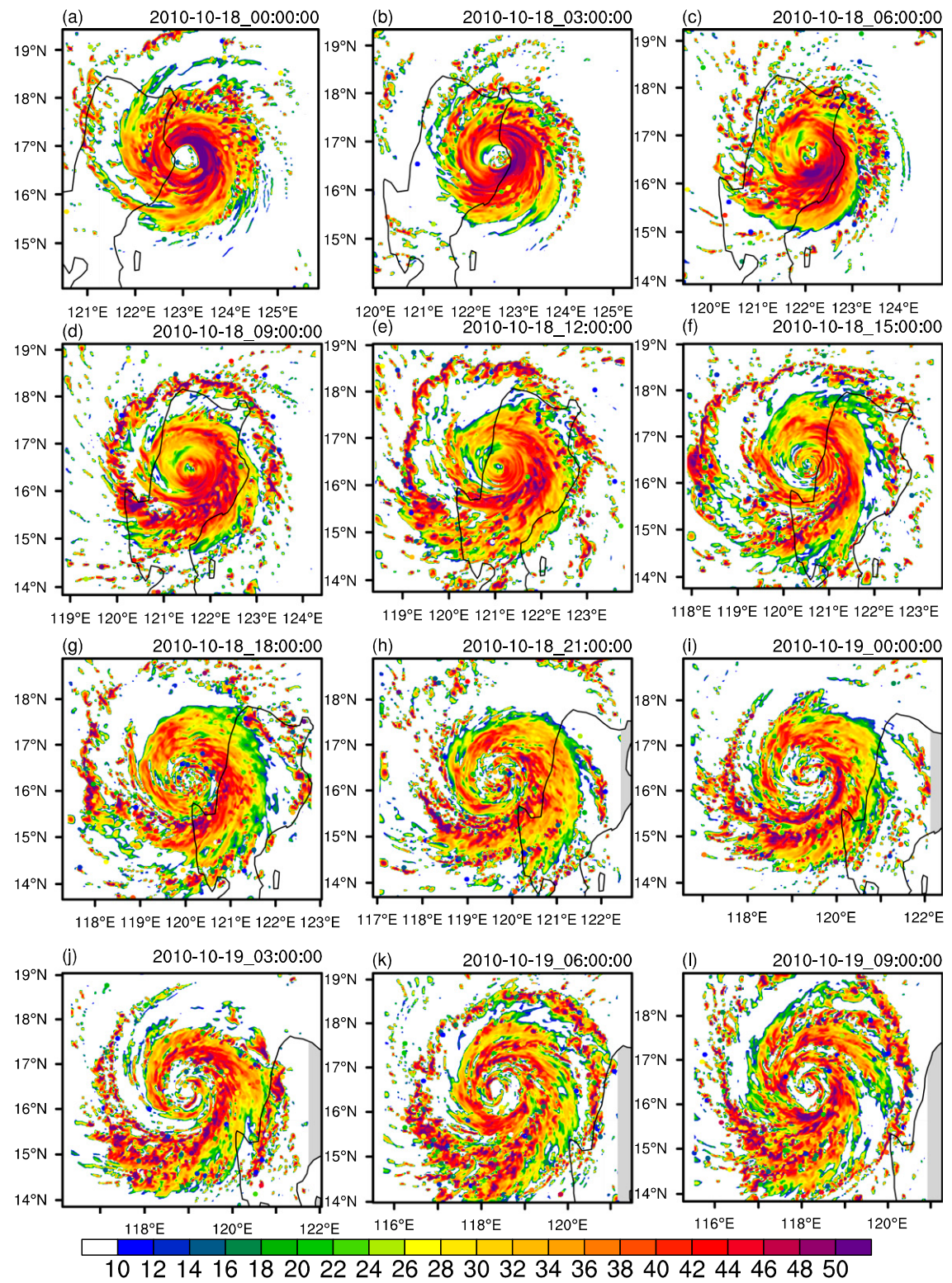


FIG. 8. As in Fig. 5, but in the experiment Notop with a flat surface over the Luzon Island.

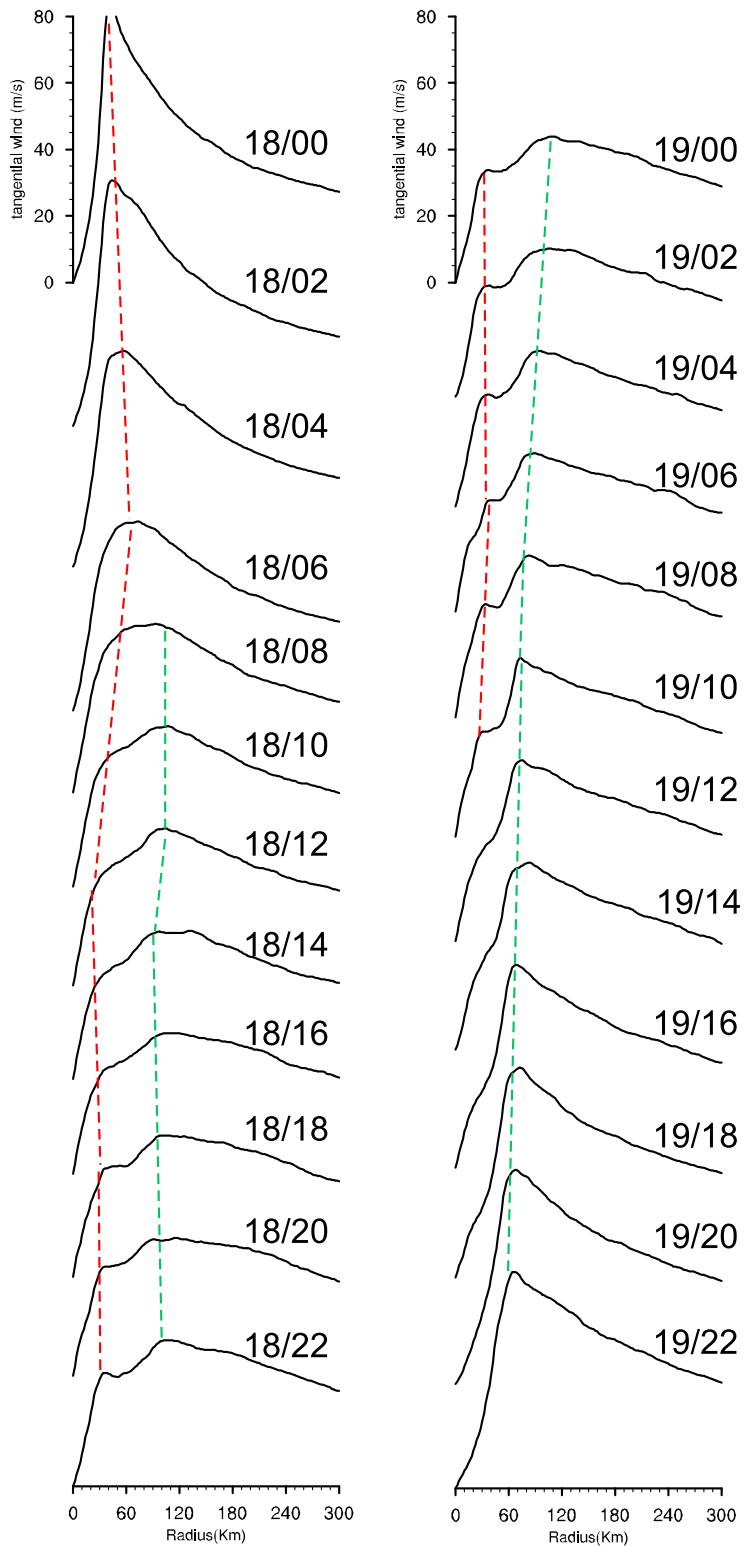


FIG. 9. As in Fig. 7, but for the simulated storm in experiment Notop.

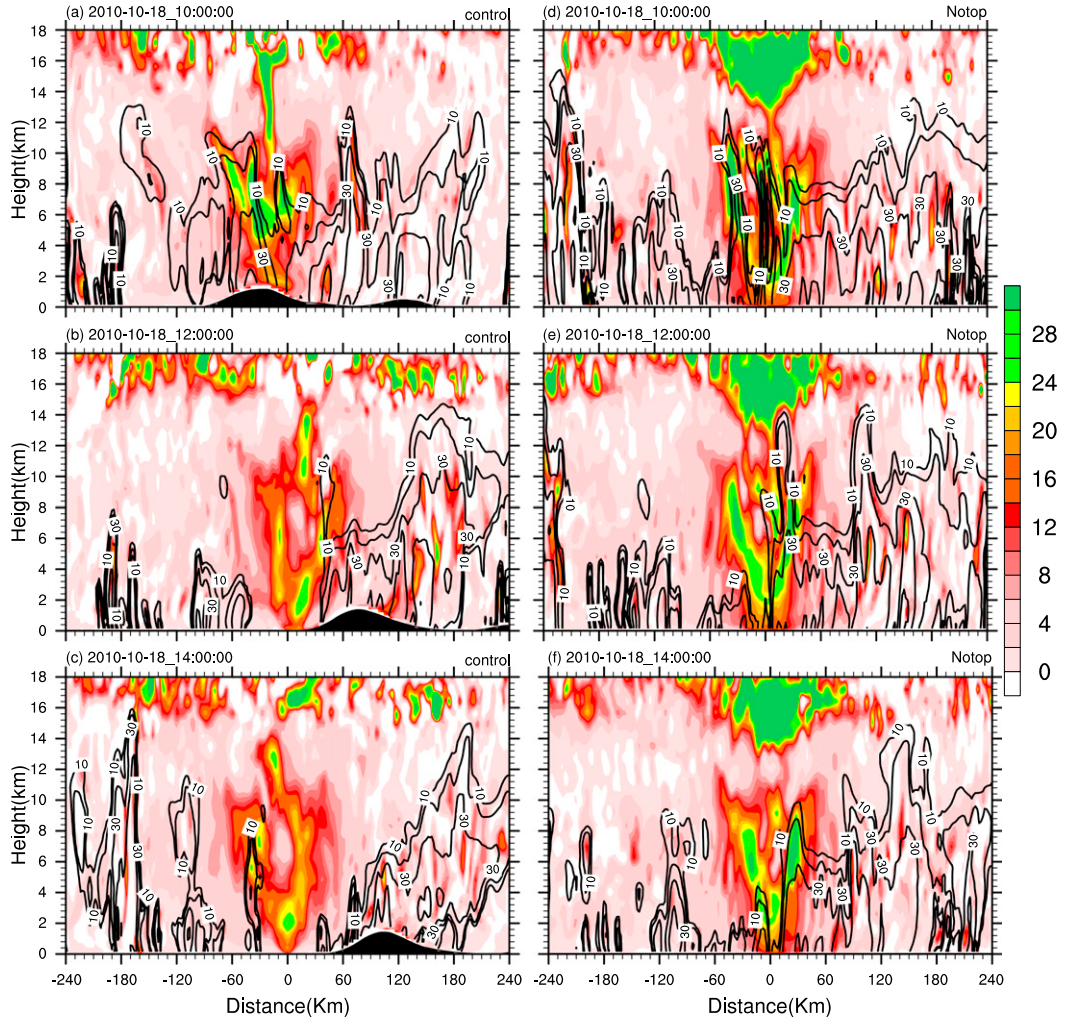


FIG. 10. West–east vertical cross section of radar reflectivity (dBZ; contours, with interval of 10 dBZ) and potential vorticity (PV; PVU, where $1 \text{ PVU} = 1 \times 10^{-6} \text{ m}^2 \text{s}^{-1} \text{ K kg}^{-1}$; shaded) through the center of the simulated Megi at (a),(d) 1000 UTC 18 Oct; (b),(e) 1200 UTC 18 Oct; and (c),(f) 1400 UTC 18 Oct in the (left) control simulation and (right) experiment Notop with a flat surface over the Luzon Island. The x axis is the distance relative to the storm center “0.”

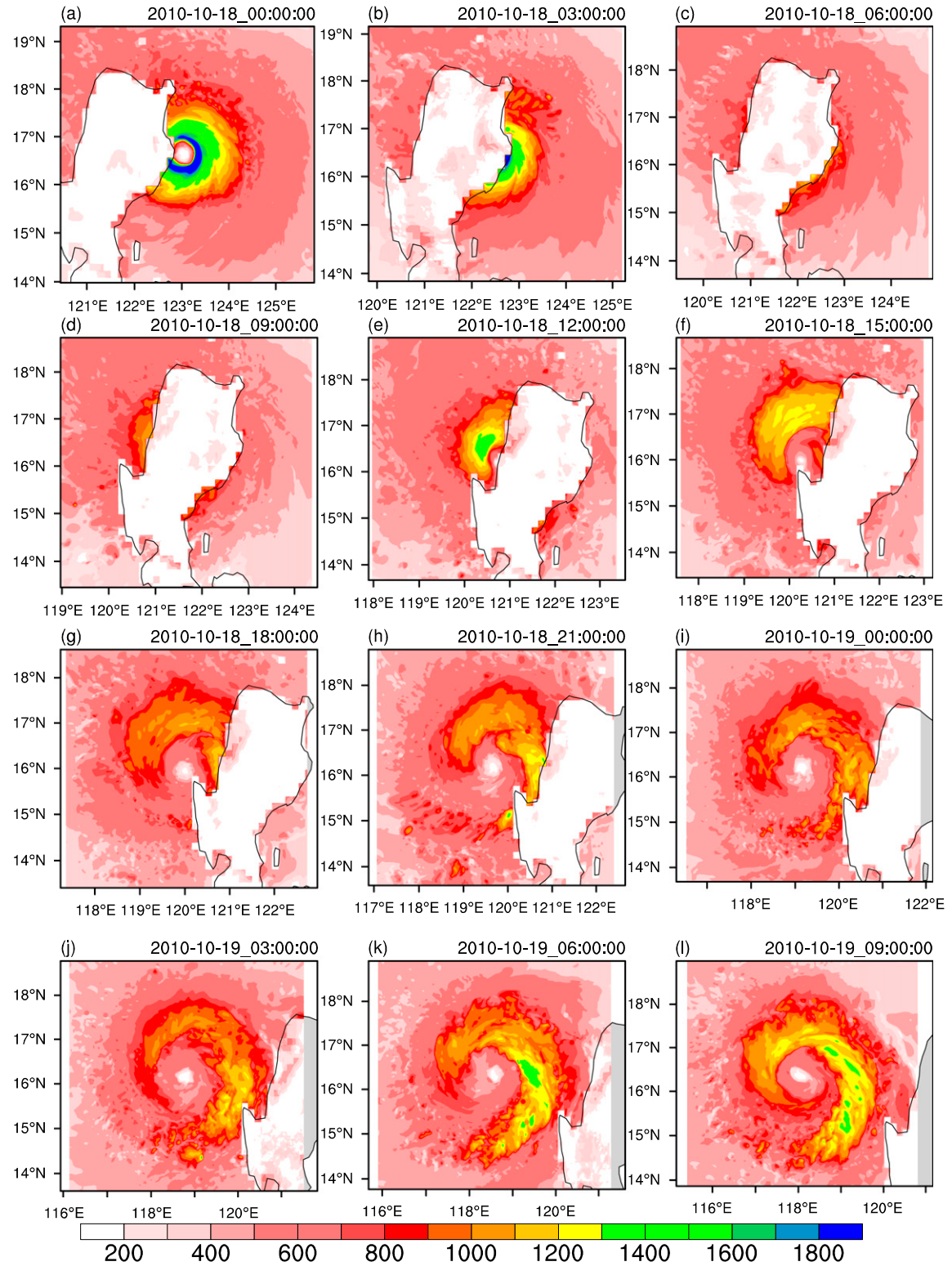
and their axisymmetrization. To demonstrate what environmental conditions favored the activity of outer spiral rainbands, we show in Figs. 11 and 12 the surface latent heat flux and convective available potential energy (CAPE) at 3-h intervals in the control experiment as shown for radar reflectivity in Fig. 5. After the storm made landfall, surface latent heat flux was largely reduced both over the Luzon Island and the surrounding oceans. After the storm center moved across the western Luzon Island, the outer core with strong winds promoted an increase in surface latent heat flux in the coastal region over the SCS (Figs. 11d–f). This increasing surface latent heat flux with moderate CAPE seemed to be responsible for the initiation of convective spiral rainbands to the northwest of the storm over the SCS as mentioned earlier (Figs. 5e–g). This rainband kept intensifying as the storm core entered the SCS and became the northern eyewall later by 0000 UTC 19 October

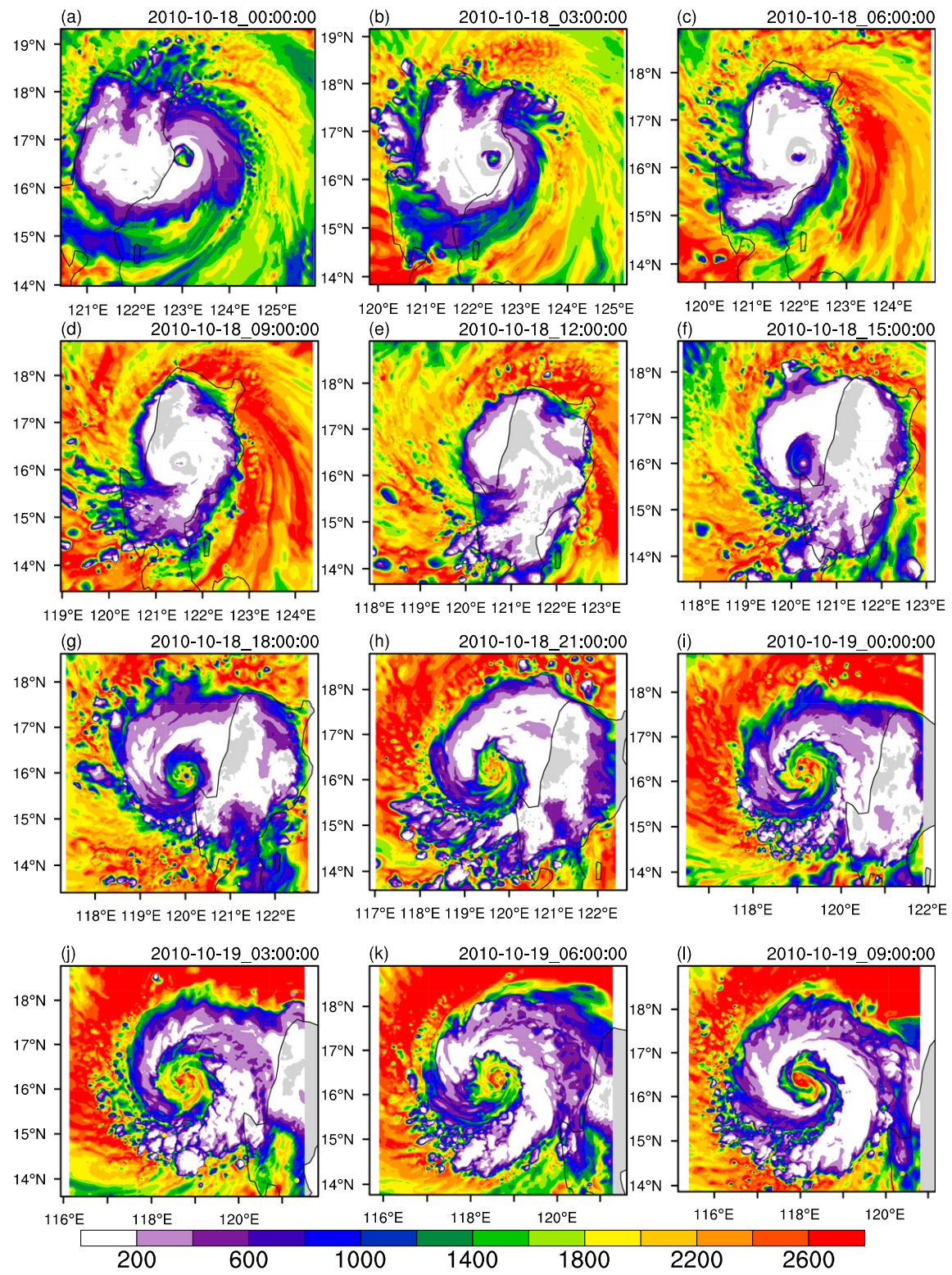
(Fig. 5i). The enhanced convective outer spiral rainband to the southwest and south of the storm center over the SCS and the Luzon Island resulted mainly from the strong outer cyclonic flow of the storm with high CAPE from the SCS (Figs. 12c–g). Note that after several hours of strong convection, CAPE in the core region started to weaken while the storm continued to intensify with the axisymmetrization of outer spiral rainbands.

To understand the axisymmetrization process, we performed the azimuthal mean tangential wind budget analysis, as done in Wang et al. (2019). The budget equation can be written as

$$\frac{\partial \bar{v}}{\partial t} = -\bar{u}\bar{\zeta}_a - \bar{w}\frac{\partial \bar{v}}{\partial z} - \bar{u}'\bar{\zeta}'_a - \bar{w}'\frac{\partial \bar{v}'}{\partial z} + \bar{F}_v, \quad (1)$$

where z is height; t is time; u , v , and w are radial and tangential winds and vertical motion, respectively; ζ_a is absolute vertical

FIG. 11. Surface latent heat flux (W m^{-2}) in the control simulation.

FIG. 12. CAPE (J kg^{-1}) in the control simulation.

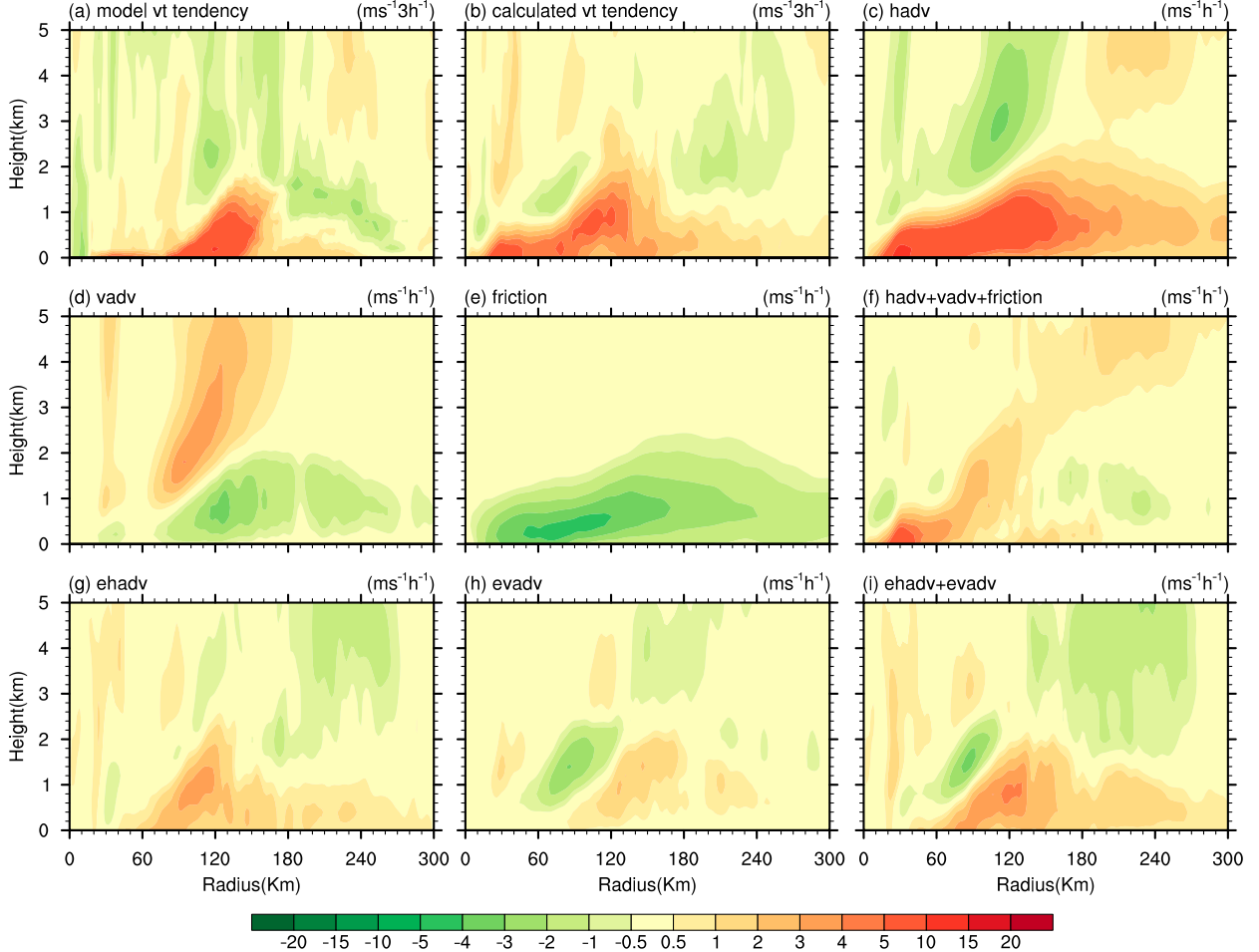


FIG. 13. The composite azimuthal mean tangential wind budget over the 3-h period from 1800 to 2100 UTC 18 Oct: (a) the actual 3-hourly change in the azimuthal mean tangential wind speed in the model; (b) the net tangential wind tendency [the sum of all terms on the rhs of (1)]; and terms related to the individual terms on the rhs of (1)—(c) mean radial flux of absolute vertical vorticity, (d) mean vertical advection, (e) mean vertical diffusion (including surface friction) term, (f) sum of the three terms associated with the azimuthal mean in (c)–(e), (g) eddy radial flux of eddy absolute vertical vorticity, (h) eddy vertical advection, and (i) the sum of the eddy terms. All terms are shown in units of meters per second per hour except for the net tangential wind tendency, which is shown in meters per second per 3 h for a direct comparison with the corresponding model tendency.

vorticity; and F_v is the vertical diffusion (including surface friction) of tangential wind. The overbar denotes the azimuthal mean, and a prime denotes the deviation from the corresponding azimuthal mean. Contributions to the tangential wind tendency on the rhs of (1) include, respectively, the mean radial flux of absolute vertical vorticity, mean vertical advection, eddy radial flux of eddy absolute vertical vorticity, eddy vertical advection, and azimuthal mean vertical diffusion (including surface friction) of tangential wind. The horizontal diffusion term is ignored because it is much smaller than any term in (1). We calculated the budget terms at every 6-min and then integrated over the 3-h period from 1800 to 2100 UTC 18 October during which the storm entered the SCS and the new large eyewall was about in the intermediate formation stage (Fig. 5). This time period was chosen to illustrate the axisymmetrization of outer spiral rainbands during the

formation of the new large eyewall as mentioned above. Figure 13 shows the results of the azimuthal mean tangential wind budget, together with the corresponding 3-h tendency of the azimuthal mean tangential wind calculated directly from the model output. Comparing Fig. 13a with Fig. 13b, we can see that the budget reproduces the tangential wind tendency simulated in the model reasonably well except for some overestimations in the eye region and beyond a radius of 240 km from the storm center in the boundary layer. The discrepancies are mainly due to the fact that the budget analysis is based on the model output at 6-min intervals not every time step. Nevertheless, the estimated tangential wind tendencies in the region of the new large eyewall formation between 120- and 180-km radii from the storm center and in the region inside a radius of 60 km where the appearance of the small inner eyewall are well captured in the budget. Therefore, results of the tangential wind budget can

help understand the role of the axisymmetrization of asymmetric structure in the formation of the new large eyewall and the small inner eyewall shortly after the storm entered and moved over the SCS.

The mean radial inflow in the boundary layer and the lower troposphere contributes to the positive azimuthal mean tangential wind tendency in both the regions of the new large eyewall formation and the appearance of the small inner eyewall (Fig. 13c). The negative tendency immediately above the positive tendency inside a radius of 150 km from the storm center indicates the spindown effect due to the outflow associated with the outward agradient force related to the upward advection of higher tangential wind from the boundary layer below (Kepert and Wang 2001; Li et al. 2020). The mean vertical advection contributes to a negative tendency in the boundary layer while a positive tendency above (Fig. 13d), indicating the upward advection of high tangential wind from the boundary layer. Note that the mean vertical advection partly offsets the tendency induced by the mean radial flux of absolute vertical vorticity. The mean vertical diffusion (including surface friction) contributes negatively to the azimuthal mean tangential wind tendencies, mainly below about 2 km height (Fig. 13e). The total contribution to the azimuthal mean tangential wind tendency by the axisymmetric processes (viz., the mean radial flux of absolute vertical vorticity, vertical advection and vertical diffusion) is shown in Fig. 13f. We can see that the net contribution by the axisymmetric processes to the azimuthal mean tangential wind spinup occurs mainly in the inner-core region inside a radius of 120 km from the storm center in the boundary layer (Fig. 13b). Interestingly, the eddy process (both eddy radial flux of vertical vorticity and eddy vertical advection, Figs. 13g and 13h) dominates the azimuthal mean tangential wind spinup in the region of the new large eyewall formation below about 2-km height (Fig. 13i). This means that eddies are more effectively axisymmetrized in the boundary layer, which is similar to the outer eyewall formation recently studied in Wang et al. (2019).

5. Appearance of the small inner eyewall

We have shown already in section 3 that it is the orographic effect of the terrain over the western Luzon Island that led to the breakdown and dissipation of the small eyewall visible earlier when the storm center moved across the terrain. As a result, a wide semicircle eyewall-like structure appeared on the windward side of the terrain (Fig. 5). After the inner core of the storm moved across the mountain over the western Luzon Island and entered the SCS, the small inner eyewall structure appeared and intensified and maintained for about 12 h, a bit longer than the observed. Similar to the classic double eyewall structure, there are two eyewalls with two maxima in the azimuthal mean tangential wind, but the maximum tangential wind of the small inner eyewall is weaker than that of the outer eyewall (Figs. 6 and 7).

The appearance of the small inner eyewall resulted most likely from the revival of the original eyewall that dissipated due to the mountain effect over the western Luzon Island as

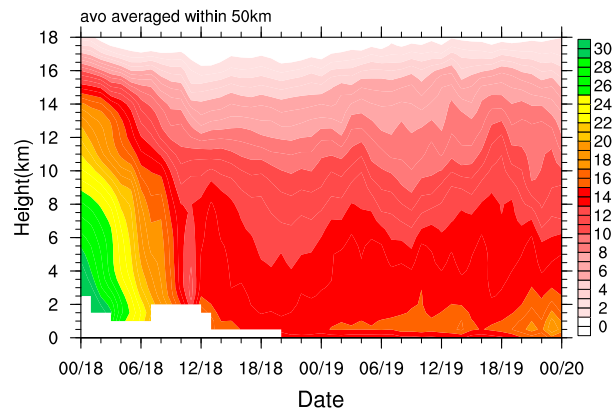


FIG. 14. The time series of relative vertical vorticity (shaded; 10^{-4} s^{-1}) averaged within 50-km radius from the storm center.

mentioned above. After the storm core entered the SCS, CAPE established in the inner-core region of the storm (Fig. 12f) and intensified with the appearance of the small inner eyewall in the following 18 h (Figs. 12g-l). The high CAPE played a key role in reviving deep convection in the inner eyewall region and the appearance of the corresponding local maximum tangential wind (Figs. 6 and 7). Different from the large outer eyewall, the appearance of the small inner eyewall and the associated deep convection did not result in the decrease of local CAPE, which in turn contributed to the maintenance of deep convection in the inner eyewall (Figs. 5 and 6). The inner eyewall eventually dissipated as the outer eyewall contracted and intensified with the reintensification of the storm over the warm SCS.

As we can see from Fig. 10a, during the inland period, the high PV core structure appeared above 4 km height while the low-level PV diminished due to the terrain effect. The storm center showed a considerable tilt at all heights shortly after the storm crossed the Luzon Island (not shown). The PV redistributed in the lower levels after the storm crossed the mountain (Fig. 10b), leading to a nearly vertically aligned high PV core in the boundary layer and lower troposphere (Fig. 10c). The redistribution of low-level PV results mainly from the reestablishment of the inner-core vorticity after the storm entered and moved over the SCS, as clearly seen from the time-height cross section of vertical relative vorticity averaged within 50 km radius from the storm center shown in Fig. 14. The averaged inner-core vorticity decreased greatly throughout the troposphere with time after landfall since 0000 UTC 18 October. Then the low-level vorticity strengthened slowly after the storm center entered the SCS. Convective cells may initiate within this low-level vorticity-rich environment under favorable thermodynamic conditions.

To understand the role of convective activities in maintaining the strength of the low to midlevel vortices, we performed a relative vorticity budget averaged in the inner-core region within 50 km from the storm center. The relative vorticity equation in the height coordinates moving with the storm can be written as

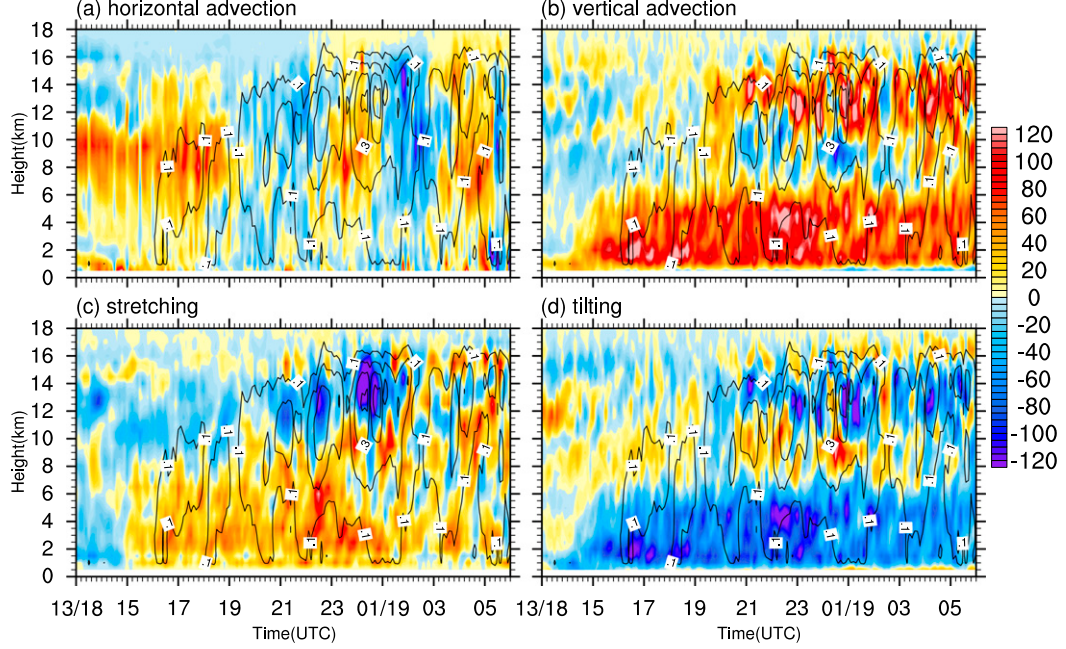


FIG. 15. Time evolution of the four terms on the rhs of (2) averaged within 50-km radius from the storm center. Shading denotes the contribution to the relative vorticity tendency (10^{-5} s^{-2}) from (a) horizontal advection, (b) vertical advection, (c) stretching, and (d) tilting. Upward motion is shown as black contours at every 0.1 m s^{-1} .

$$\begin{aligned} \frac{\partial \zeta}{\partial t} \Big|_{\text{MV}} = & -(\mathbf{V}_h - \mathbf{C}) \cdot \nabla_h (\zeta + f) - w \frac{\partial \zeta}{\partial z} - (\zeta + f) \nabla_h \cdot (\mathbf{V}_h - \mathbf{C}) \\ & - \left(\frac{\partial w}{\partial x} \frac{\partial v}{\partial z} - \frac{\partial w}{\partial y} \frac{\partial u}{\partial z} \right) + \frac{1}{\rho^2} \left(\frac{\partial \rho}{\partial x} \frac{\partial p}{\partial y} - \frac{\partial \rho}{\partial y} \frac{\partial p}{\partial x} \right) + \frac{\partial F_y}{\partial x} - \frac{\partial F_x}{\partial y}, \end{aligned} \quad (2)$$

where ζ is the relative vertical vorticity, \mathbf{C} is the motion vector of the vortex, \mathbf{V}_h is the horizontal wind vector, ρ is air density, p is air pressure, F_x and F_y are the vertical diffusion terms of zonal and meridional winds, and the subscript MV denotes that the budget is calculated in the reference moving with the storm center. The term on the lhs in (2) is the local relative vorticity tendency (TEN), and terms on the rhs are respectively horizontal vorticity advection (HAV), vertical vorticity advection (VAD), the stretching term (STR), the tilting term (TIL), the solenoidal term (SOL), and the vertical diffusion term. In the results discussed below, all terms are horizontally averaged within 50 km radius from the storm center. We have done a budget for the period from 1300 UTC 18 October to 0600 UTC 19 October, during which the small inner eyewall gradually appeared with active convection first (Fig. 5) and its local maximum azimuthal mean tangential wind in the boundary layer (Figs. 6 and 7).

Figure 15 shows the time evolution of the first four terms on the rhs in (2). We can see that the horizontal advection contributes to the increase in vertical relative vorticity mainly in the middle troposphere when the storm center initially entered the SCS but seems to play a secondary role afterward (Fig. 15a). The vertical advection contributes vertical relative vorticity positively in the lower and upper troposphere throughout the

time period but negatively in the midlevels (Fig. 15b). The stretching term is positive in the mid- to lower troposphere and mostly negative in the upper troposphere. The titling term contributes negatively in the lower and upper troposphere but positively in the middle troposphere (Fig. 15d), nearly opposite to the contribution by vertical advection. As a result, the vertical advection and titling terms largely cancel each other. Therefore, the steady increase in low-level relative vertical vorticity is largely due to the stretching term or the low-level convergence, which was partly enhanced by the reinitiated convection near the circulation center. The low-level convergence stretched the inner-core environmental vorticity and enhanced upward motion in the mid- to lower troposphere through vertical stretching. This would enhance convection, and convective heating could in turn further enhance the low-level convergence and vorticity stretching. This positive feedback contributed to the revival of active convection and thus the appearance of the small inner eyewall. The importance of stretching term is also reflected in the azimuthal mean tangential wind budget discussed in section 4. Namely, the appearance of the local maximum in the azimuthal mean tangential wind in the boundary layer was largely contributed by the boundary layer inflow, which also contributed to the increase in low-level vertical relative vorticity by stretching term. This process was interrupted later as the new large outer eyewall formed and contracted and intensified, eventually leading to the disappearance of the inner eyewall and completing the eyewall replacement cycle.

The above analysis suggests that the appearance of the small inner eyewall and the reintensification of the storm were

explained from three processes. First, the high SST over the SCS favored the establishment of high CAPE in the central region of the storm (Fig. 12). Second, the elevated surface latent heat flux (Fig. 11) and high CAPE contribute to reinvigorating convection close to the surface circulation center (Figs. 5, 11, and 12). Third, the boundary layer convergence enhanced by the reviving convection helped spin up the tangential wind and enhance low-level vorticity, and thus the appearance of the local tangential wind maximum under the small inner eyewall. A positive feedback occurs between the low-level convergence and convection through vorticity stretching. These processes can also be seen from Figs. 5 and 6. The initiation of deep convection and thus deep diabatic heating appeared near a radius of 30 km in the central region of the storm (Figs. 6f–i) before the appearance of the local maximum in the azimuthal mean tangential wind (Fig. 6j). With the terrain removed in experiment Notop, the inner eyewall did not disappear when the storm moved across the Luzon Island but strengthened after the storm entered the SCS (Fig. 8). This further demonstrates that the terrain over the western Luzon Island played an important role in the eyewall evolution of the simulated Megi when it crossed the Luzon Island.

6. Conclusions

Typhoon Megi (2010) experienced a drastic eyewall evolution when it crossed the Luzon Island over the northern Philippines and entered the SCS, including the contraction and breakdown of the eyewall after landfall, the formation of a new large eyewall accompanied by reintensification of the storm after it entered the SCS, and the appearance of a short-lived small inner eyewall. These features were reproduced reasonably well in a control simulation using the ARW-WRF Model with both dynamical TC initialization and large-scale spectral nudging (Wang et al. 2013; Part I). In this part, the eyewall evolution of the simulated Typhoon Megi has been analyzed. The results show that the presence of the landmass of Luzon Island was responsible for the weakening of Typhoon Megi when it crossed the Luzon Island. The steep mountain over the western Luzon Island played a critical role in causing the breakdown and dissipation of the original eyewall of the storm during the postlandfall period.

Both the increased surface friction and reduced surface enthalpy flux were responsible for the weakening of the storm and also led to the eyewall to contract and break down when the storm crossed the Luzon Island. The new large eyewall formed as a result of the axisymmetrization of two outer spiral rainbands after the storm core crossed the Luzon Island and entered the SCS. An interesting feature was the appearance of the small inner eyewall after the simulated storm core entered the SCS, which was contributed by the favorable environmental (oceanic) conditions, including the high SST and thus CAPE over the SCS. The high SST over the SCS and the relatively high surface winds in the inner core region led to the increase in surface enthalpy flux and high CAPE. As a result, convection in the weakened inner core revived and developed into a nearly ring-like structure. This further enhances the low-level convergence and inward transport of angular momentum,

leading to the increase in both the azimuthal mean tangential wind and the upward motion by vertical stretching of inner-core environmental vorticity. Eventually, the revived eyewall had its own local maximum azimuthal mean wind and deep convection although the maximum wind speed was weaker than the newly formed large outer eyewall. As the large outer eyewall contracted and intensified, the small inner eyewall weakened and dissipated after about 12 h in the simulation, which was about 3 h longer than that in the observed Megi.

Results from two sensitivity experiments demonstrate that the eyewall evolution of Megi was largely contributed by the mesoscale mountain over the western Luzon Island. With the mesoscale mountain replaced by a flat surface over the Luzon Island, convection in the outer eyewall was active over the western Luzon Island, and the size of the eyewall was reduced by one-third relative to that in the control experiment with terrain unchanged after the storm core entered the SCS. This demonstrates that the large size of the new (outer) eyewall was also partially associated with the orographic forcing over the western Luzon Island. Although some similar eyewall evolution features for a TC crossing the Luzon Island have been documented in previous studies (e.g., Wu et al. 2003, 2009; Chou et al. 2011), this study documents a new feature that has not been discussed in the literature, namely the appearance of the small inner eyewall after the storm crossed the Luzon Island and entered the SCS. In the classic double eyewall structure, often a secondary eyewall forms outside the primary eyewall. The appearance of the small inner eyewall after the formation of the large outer eyewall in Megi led to the concentric eyewall structure. In this sense, this is a new category of secondary eyewall formation; namely, a new secondary eyewall appeared in an existing large outer eyewall. However, the subsequent evolution of the concentric eyewall, that is, the eyewall replacement cycle, is similar to the classic eyewall replacement cycle.

Acknowledgments. The authors are grateful to three anonymous reviewers whose review comments helped to improve the paper. This study has been supported in part by the National Key R&D Program of China under Grant 2017YFC1501602; the National Natural Science Foundation of China under Grants 41730960, 41675047, and 41675044; and in part by NSF Grant AGS-1834300. The 85-GHz images in Fig. 3 were obtained online (http://www.nrlmry.navy.mil/sat_training/tropical_cyclones/ssmi/85h/index.html).

REFERENCES

- Brand, S., and J. W. Bleloch, 1973: Changes in the characteristics of typhoons crossing the Philippines. *J. Appl. Meteor.*, **12**, 104–109, [https://doi.org/10.1175/1520-0450\(1973\)012<104:COTC>2.0.CO;2](https://doi.org/10.1175/1520-0450(1973)012<104:COTC>2.0.CO;2).
- Chou, K.-H., C.-C. Wu, Y. Wang, and C.-H. Chih, 2011: Eyewall evolution of typhoons crossing the Philippines and Taiwan: An observational study. *Terr. Atmos. Oceanic Sci.*, **22**, 535–548, [https://doi.org/10.3319/TAO.2011.05.10.01\(TM\)](https://doi.org/10.3319/TAO.2011.05.10.01(TM)).
- Didlake, A. C., Jr., and R. A. Houze Jr., 2011: Kinematics of the secondary eyewall observed in Hurricane Rita (2005). *J. Atmos. Sci.*, **68**, 1620–1636, <https://doi.org/10.1175/2011JAS3715.1>.

- , P. D. Reasor, R. F. Rogers, and W.-C. Lee, 2018: Dynamics of the transition from spiral rainbands to a secondary eyewall in Hurricane Earl (2010). *J. Atmos. Sci.*, **75**, 2909–2929, <https://doi.org/10.1175/JAS-D-17-0348.1>.
- Hawkins, H. F., 1983: Hurricane Allen and island obstacles. *J. Atmos. Sci.*, **40**, 1360–1361, [https://doi.org/10.1175/1520-0469\(1983\)040<1360:HAAIO>2.0.CO;2](https://doi.org/10.1175/1520-0469(1983)040<1360:HAAIO>2.0.CO;2).
- Hendricks, E. A., and W. H. Schubert, 2010: Adiabatic rearrangement of hollow PV towers. *J. Adv. Model. Earth Syst.*, **2**, 8, <https://doi.org/10.3894/JAMES.2010.2.8>.
- , —, R. K. Taft, H. Wang, and J. P. Kossin, 2009: The life cycles of hurricane-like vorticity rings. *J. Atmos. Sci.*, **66**, 705–722, <https://doi.org/10.1175/2008JAS2820.1>.
- Houze, R. A., Jr., S. S. Chen, B. F. Smull, W.-C. Lee, and M. M. Bell, 2007: Hurricane intensity and eyewall cycle. *Science*, **315**, 1235–1239, <https://doi.org/10.1126/science.1135650>.
- Hsu, L.-H., H.-C. Kuo, and R. G. Fovell, 2013: On the geographic asymmetry of typhoon translation speed across the mountainous island of Taiwan. *J. Atmos. Sci.*, **70**, 1006–1022, <https://doi.org/10.1175/JAS-D-12-0173.1>.
- Huang, Y.-H., C.-C. Wu, and Y. Wang, 2011: The influence of island topography on typhoon track deflection. *Mon. Wea. Rev.*, **139**, 1708–1727, <https://doi.org/10.1175/2011MWR3560.1>.
- , M. T. Montgomery, and C.-C. Wu, 2012: Concentric eyewall formation in Typhoon Sinlaku (2008). Part II: Axisymmetric dynamical processes. *J. Atmos. Sci.*, **69**, 662–674, <https://doi.org/10.1175/JAS-D-11-0114.1>.
- Kepert, J. D., and Y. Wang, 2001: The dynamics of boundary layer jets within the tropical cyclone core. Part II: Nonlinear enhancement. *J. Atmos. Sci.*, **58**, 2485–2501, [https://doi.org/10.1175/1520-0469\(2001\)058<2485:TDOBLJ>2.0.CO;2](https://doi.org/10.1175/1520-0469(2001)058<2485:TDOBLJ>2.0.CO;2).
- Knaff, J. A., J. P. Kossin, and M. DeMaria, 2003: Annular hurricanes. *Wea. Forecasting*, **18**, 204–223, [https://doi.org/10.1175/1520-0434\(2003\)018<0204:AH>2.0.CO;2](https://doi.org/10.1175/1520-0434(2003)018<0204:AH>2.0.CO;2).
- Kossin, J. P., and M. D. Eastin, 2001: Two distinct regimes in the kinematic and thermodynamic structure of the hurricane eye and eyewall. *J. Atmos. Sci.*, **58**, 1079–1090, [https://doi.org/10.1175/1520-0469\(2001\)058<1079:TDRITK>2.0.CO;2](https://doi.org/10.1175/1520-0469(2001)058<1079:TDRITK>2.0.CO;2).
- , and W. H. Schubert, 2001: Mesovortices, polygonal flow patterns, and rapid pressure falls in hurricane-like vortices. *J. Atmos. Sci.*, **58**, 2196–2209, [https://doi.org/10.1175/1520-0469\(2001\)058<2196:MPFPAR>2.0.CO;2](https://doi.org/10.1175/1520-0469(2001)058<2196:MPFPAR>2.0.CO;2).
- , and M. Sitkowski, 2009: An objective model for identifying secondary eyewall formation in hurricanes. *Mon. Wea. Rev.*, **137**, 876–892, <https://doi.org/10.1175/2008MWR2701.1>.
- Kuo, H.-C., C.-P. Chang, Y.-T. Yang, and H.-J. Jiang, 2009: Western North Pacific typhoons with concentric eyewalls. *Mon. Wea. Rev.*, **137**, 3758–3770, <https://doi.org/10.1175/2009MWR2850.1>.
- Li, Y.-L., Y. Wang, and Y.-L. Lin, 2020: How much does the upward advection of supergradient component of boundary layer wind contribute to tropical cyclone intensification and maximum intensity? *J. Atmos. Sci.*, **77**, 2649–2664, <https://doi.org/10.1175/JAS-D-19-0350.1>.
- Lin, S.-J., and K.-H. Chou, 2018: Characteristics of size change of tropical cyclones traversing the Philippines. *Mon. Wea. Rev.*, **146**, 2891–2911, <https://doi.org/10.1175/MWR-D-18-0004.1>.
- Lin, Y.-L., D. B. Ensley, S. Chiao, and C.-Y. Huang, 2002: Orographic influences on rainfall and track deflection associated with the passage of a tropical cyclone. *Mon. Wea. Rev.*, **130**, 2929–2950, [https://doi.org/10.1175/1520-0493\(2002\)130<2929:OIORAT>2.0.CO;2](https://doi.org/10.1175/1520-0493(2002)130<2929:OIORAT>2.0.CO;2).
- , N. C. Witcraft, and Y.-H. Kuo, 2006: Dynamics of track deflection associated with the passage of tropical cyclones over a mesoscale mountain. *Mon. Wea. Rev.*, **134**, 3509–3538, <https://doi.org/10.1175/MWR3263.1>.
- Maclay, K. S., M. DeMaria, and T. H. V. Haar, 2008: Tropical cyclone inner-core kinetic energy evolution. *Mon. Wea. Rev.*, **136**, 4882–4898, <https://doi.org/10.1175/2008MWR2268.1>.
- Rozoff, C. M., J. P. Kossin, W. H. Schubert, and P. J. Mulero, 2009: Internal control of hurricane intensity variability: The dual nature of potential vorticity mixing. *J. Atmos. Sci.*, **66**, 133–147, <https://doi.org/10.1175/2008JAS2717.1>.
- Schubert, W. H., M. T. Montgomery, R. K. Taft, T. A. Quinn, S. R. Fulton, J. P. Kossin, and J. P. Edwards, 1999: Polygonal eyewalls, asymmetric eye contraction, and potential vorticity mixing in hurricanes. *J. Atmos. Sci.*, **56**, 1197–1223, [https://doi.org/10.1175/1520-0469\(1999\)056<1197:PEAECA>2.0.CO;2](https://doi.org/10.1175/1520-0469(1999)056<1197:PEAECA>2.0.CO;2).
- Sitkowski, M., J. P. Kossin, and C. M. Rozoff, 2011: Intensity and structure changes during hurricane eyewall replacement cycles. *Mon. Wea. Rev.*, **139**, 3829–3847, <https://doi.org/10.1175/MWR-D-11-00034.1>.
- Skamarock, W. C. and Coauthors, 2008: A description of the Advanced Research WRF version 3. NCAR Tech. Note NCAR/TN-475+STR, 113 pp., <https://doi.org/10.5065/D68S4MVH>.
- Tang, C. K., and J. C. L. Chan, 2014: Idealized simulations of the effect of Taiwan and Philippines topographies on tropical cyclone tracks. *Quart. J. Roy. Meteor. Soc.*, **140**, 1578–1589, <https://doi.org/10.1002/qj.2240>.
- , and —, 2016: Idealized simulations of the effect of Taiwan topography on the tracks of tropical cyclones with different steering flow strengths. *Quart. J. Roy. Meteor. Soc.*, **142**, 3211–3221, <https://doi.org/10.1002/qj.2902>.
- Wang, H., and Y. Wang, 2014: A numerical study of Typhoon Megi (2010). Part I: Rapid intensification. *Mon. Wea. Rev.*, **142**, 29–48, <https://doi.org/10.1175/MWR-D-13-00070.1>.
- , —, and H.-M. Xu, 2013: Improving simulation of a tropical cyclone using dynamical initialization and large-scale spectral nudging: A case study of Typhoon Megi (2010). *Acta Meteor. Sin.*, **27**, 455–475, <https://doi.org/10.1007/s13351-013-0418-y>.
- , C. Wu, and Y. Wang, 2016: Secondary eyewall formation in an idealized tropical cyclone simulation: Balanced and unbalanced dynamics. *J. Atmos. Sci.*, **73**, 3911–3930, <https://doi.org/10.1175/JAS-D-15-0146.1>.
- , Y. Wang, J. Xu, and Y.-H. Duan, 2019: The axisymmetric and asymmetric aspects of the secondary eyewall formation in a numerically simulated tropical cyclone under idealized conditions on an f plane. *J. Atmos. Sci.*, **76**, 357–378, <https://doi.org/10.1175/JAS-D-18-0130.1>.
- Wang, Y., 2002a: Vortex Rossby waves in a numerically simulated tropical cyclone. Part I: Overall structure, potential vorticity, and kinetic energy budgets. *J. Atmos. Sci.*, **59**, 1213–1238, [https://doi.org/10.1175/1520-0469\(2002\)059<1213:VRWIAN>2.0.CO;2](https://doi.org/10.1175/1520-0469(2002)059<1213:VRWIAN>2.0.CO;2).
- , 2002b: Vortex Rossby waves in a numerically simulated tropical cyclone. Part II: The role in tropical cyclone structure and intensity changes. *J. Atmos. Sci.*, **59**, 1239–1262, [https://doi.org/10.1175/1520-0469\(2002\)059<1239:VRWIAN>2.0.CO;2](https://doi.org/10.1175/1520-0469(2002)059<1239:VRWIAN>2.0.CO;2).
- , 2009: How do outer spiral rainbands affect tropical cyclone structure and intensity? *J. Atmos. Sci.*, **66**, 1250–1273, <https://doi.org/10.1175/2008JAS2737.1>.

- , 2012: Recent research progress on tropical cyclone structure and intensity. *Trop. Cyclone Res. Rev.*, **1**, 254–275, <https://doi.org/10.6057/2012TCRR02.05>.
- , and C.-C. Wu, 2004: Current understanding of tropical cyclone structure and intensity changes—A review. *Meteor. Atmos. Phys.*, **87**, 257–278, <https://doi.org/10.1007/s00703-003-0055-6>.
- Wei, C. C., 2014: Surface wind nowcasting in the Penghu Islands based on classified typhoon tracks and the effects of the central mountain range of Taiwan. *Wea. Forecasting*, **29**, 1425–1450, <https://doi.org/10.1175/WAF-D-14-00027.1>.
- Willoughby, H. E., and P. G. Black, 1996: Hurricane Andrew in Florida: Dynamics of disaster. *Bull. Amer. Meteor. Soc.*, **77**, 543–549, [https://doi.org/10.1175/1520-0477\(1996\)077<0543:HAIFDO>2.0.CO;2](https://doi.org/10.1175/1520-0477(1996)077<0543:HAIFDO>2.0.CO;2).
- , J. A. Clos, and M. G. Shoreibah, 1982: Concentric eyewalls, secondary wind maximum, and the evolution of the hurricane vortex. *J. Atmos. Sci.*, **39**, 395–411, [https://doi.org/10.1175/1520-0469\(1982\)039<0395:CEWSWM>2.0.CO;2](https://doi.org/10.1175/1520-0469(1982)039<0395:CEWSWM>2.0.CO;2).
- Wu, C.-C., 2013: Typhoon Morakot: Key findings from the journal TAO for improving prediction of extreme rains at landfall. *Bull. Amer. Meteor. Soc.*, **94**, 155–160, <https://doi.org/10.1175/BAMS-D-11-00155.1>.
- , and Y.-H. Kuo, 1999: Typhoons affecting Taiwan: Current understanding and future challenges. *Bull. Amer. Meteor. Soc.*, **80**, 67–80, [https://doi.org/10.1175/1520-0477\(1999\)080<0067:TATCUA>2.0.CO;2](https://doi.org/10.1175/1520-0477(1999)080<0067:TATCUA>2.0.CO;2).
- , K.-H. Chou, H.-J. Cheng, and Y. Wang, 2003: Eyewall contraction, breakdown and reformation in a landfalling typhoon. *Geophys. Res. Lett.*, **30**, 1887, <https://doi.org/10.1029/2003GL017653>.
- , H.-J. Cheng, Y. Wang, and K.-H. Chou, 2009: A numerical investigation of the eyewall evolution of a landfalling typhoon. *Mon. Wea. Rev.*, **137**, 21–40, <https://doi.org/10.1175/2008MWR2516.1>.
- Yang, B., Y. Wang, and B. Wang, 2007: The effect of internally generated inner-core asymmetries on tropical cyclone potential intensity. *J. Atmos. Sci.*, **64**, 1165–1188, <https://doi.org/10.1175/JAS3971.1>.
- Yang, M.-J., D.-L. Zhang, and H.-L. Huang, 2008: A modeling study of Typhoon Nari (2001) at landfall. Part I: Topographic effects. *J. Atmos. Sci.*, **65**, 3095–3115, <https://doi.org/10.1175/2008JAS2453.1>.